

# Modeling and computation of unsteady cavitation flows in injection nozzles

Weixing Yuan, Jürgen Sauer, Günter H. Schnerr\*

*Fachgebiet Strömungsmaschinen, University of Karlsruhe (TH), Kaiserstr. 12, D-76128 Karlsruhe, Germany*

(Received 30 April 2001; accepted 1 June 2001)

**Abstract**—This paper deals with the numerical simulation of cavitation phenomena inside injector nozzles. The numerical approach combines the Volume-of-Fluid technique (VOF) with a model predicting the growth and collapse of bubbles. To model the turbulence effect a  $k-\omega$  model is introduced for the two-phase flow. Calculations show that the numerical method is able to reproduce complex cavitation phenomena as observed in injection nozzle experiments. © 2001 Éditions scientifiques et médicales Elsevier SAS

**cavitation / injection nozzle / numerical simulation / dispersed two-phase microhydrodynamics / bubble growth / separation**

**Résumé**—Cet article traite de la simulation numérique du phénomène de cavitation dans les tuyères d'injection. L'approche numérique combine la technique «Volume-of-Fluid» à un modèle de prédiction du développement et du collapse des bulles. Les équations de Navier–Stokes décrivant l'écoulement biphase, sont utilisées. De plus, le modèle  $k-\omega$  est adopté pour la modélisation de la turbulence. Les calculs montrent que la méthode numérique est capable de reproduire les phénomènes complexes de cavitation, observés expérimentalement dans les tuyères d'injection. © 2001 Éditions scientifiques et médicales Elsevier SAS

**cavitation / injecteurs / simulation numérique / microhydrodynamique diphasique / croissance de bulles / separation**

## 1. INTRODUCTION

Control and optimization of the flow through injector nozzles are important because they affect the spray formation, the atomization process of the liquid fuel and, therefore, the efficiency and emission of the combustion process. The dominating characteristics of the underlying fluid dynamic problem are unsteadiness, caused by instantaneously very high pressure pulses, nonequilibrium effects due to very high flow velocities and the small scale of typical nozzles of  $10^{-4}$ – $10^{-3}$  m, etc. Experimental visualizations have shown that the strong suction peak at the nozzle inlet initiates local evaporation of the liquid forming so-called cavitation sheets which become unstable further downstream with unsteady break-off of vapor clouds [1]. Spray measurements outside of the nozzle have shown that cavitation inside the nozzle

causes a substantial change of relevant spray characteristics [2].

Currently, time accurate solutions of flows through injector nozzles are of great interest, since the small size of the nozzle and the high velocity of the flow make experimental measurements of this internal flow extremely difficult. Our main interest concerns numerical simulations of fully developed cavitation phenomena inside the nozzle. The present numerical approach to the solution of cavitation bases on a combination of the Volume-of-Fluid technique (VOF), originally developed for capturing of free surfaces [3], i.e. for two-phase flows without phase transition [4], with an additional model for the growth and collapse of bubbles [5]. From the macroscopic view we calculate time dependent vapor distributions. However, depending on the individual bubble growth model, we resolve the spatial and time dependent bubble size distribution. To model the turbulence effect a  $k-\omega$  model [6] is introduced for the cavitating flow. A finite-volume approach is used for the numerical discretization. Several complex cavitation phenomena are obtained using the present method.

\* Correspondence and reprints.

*E-mail address:* guenter.schnerr@mach.uni-karlsruhe.de  
(G.H. Schnerr).

## 2. MATHEMATICAL AND NUMERICAL MODEL

### 2.1. Governing equations

The bubble–liquid flow is treated as a homogeneous vapor–liquid mixture, hence only one set of equations is used for description. The continuity equation, together with the momentum equations, are listed as follows:

$$\frac{\partial \rho}{\partial t} + \text{div}(\rho \vec{c}) = 0 \quad (1)$$

$$\frac{\partial(\rho \vec{c})}{\partial t} + \text{div} \left[ \rho \vec{c} \vec{c} + \left( p + \frac{2}{3} \mu \text{div} \vec{c} \right) \vec{I} \right] = 2\mu \text{div} \vec{D} \quad (2)$$

where  $t$  stands for time,  $\vec{c}$  for the velocity,  $p$  for the static pressure.  $\vec{I}$  is the unit tensor and  $\vec{D}$  is the rate of strain (deformation) tensor. The equations of motion are closed with the constitutive relations for the density  $\rho$  and the dynamic viscosity  $\mu$ :

$$\begin{aligned} \rho &= (1 - \alpha)\rho_l + \alpha\rho_v \\ \mu &= (1 - \alpha)\mu_l + \alpha\mu_v \end{aligned} \quad (3)$$

where  $\alpha$  is the vapor fraction. The subscripts  $l$  and  $v$  stand for the properties of pure liquid and pure vapor which are assumed to be constant. In the case that the turbulence modeling is carried out,  $\mu_{\text{eff}}$  is used instead of the molecular viscosity  $\mu$ :

$$\mu_{\text{eff}} = \mu + \mu_t \quad (4)$$

where  $\mu_t$  represents the turbulence viscosity which is modeled using the Wilcox  $k$ - $\omega$  model [6], see Section 2.3.

### 2.2. Bubble growth model

To close the system of equations, an additional relation is needed since we have introduced a new variable  $\alpha$ . As proposed in [7] the vapor is assumed to consist of mini spherical bubbles, thus the vapor fraction can be calculated as

$$\alpha = \frac{n_0 \cdot 4\pi R^3/3}{1 + n_0 \cdot 4\pi R^3/3} \quad (5)$$

where  $R$  is the bubble radius and  $n_0$  is defined as nuclei concentration per unit volume of pure liquid.

Bubble growth rates have been investigated since the beginning of the last century [5, 8]. The simplest but very effective description for the bubble growth is the Rayleigh relation [5] which is widely used in numerical computation, e.g., [9]:

$$\dot{R} = \frac{dR}{dt} = \sqrt{\frac{2}{3} \frac{p(R) - p_\infty}{\rho_l}} \quad (6)$$

where  $p(R)$  is the pressure in the liquid at the bubble boundary and  $p_\infty$  is the pressure at a large distance from the bubble. This relation is applicable in the range of moderately low pressures. In this study,  $p(R)$  is set equal to the equilibrium vapor pressure  $p_{\text{vap}}$  and  $p_\infty$  to the ambient cell pressure. Using this assumption we can calculate the vapor production rate from the following equation:

$$\frac{d\alpha}{dt} = (1 - \alpha) \frac{4\pi n_0 R^2 \dot{R}}{1 + n_0 \cdot 4\pi R^3/3} \quad (7)$$

To overcome numerical difficulties due to the strong variation of the density between the liquid and vapor phase, as proposed in [7, 10], we use the so-called nonconservative form of the continuity equation with the advantage of continuous volume fluxes at the cell interfaces:

$$\nabla \cdot \vec{c} = \frac{-1}{\rho} \left( \frac{\partial \rho}{\partial t} + \vec{c} \cdot \nabla \rho \right) = \frac{-1}{\rho} \frac{d\rho}{dt} = \frac{\rho_l - \rho_v}{\rho} \frac{d\alpha}{dt} \quad (8)$$

This nonconservative continuity equation is solved together with the momentum equation (Eq. (2)) by a pressure correction method, here a modified SIMPLE algorithm. The additional term of  $d\alpha/dt$  is zero for flows without mass transfer between the flow phases. For the vapor fraction  $\alpha$  we derive the following transport equation which is a variant of the continuity equation (Eq. (1)) together with Eqs. (7), (8):

$$\begin{aligned} \frac{\partial \alpha}{\partial t} + \nabla \cdot (\alpha \vec{c}) &= \frac{d\alpha}{dt} + \alpha \nabla \cdot \vec{c} \\ &= \frac{(1 - \alpha)\rho_l}{(1 - \alpha)\rho_l + \alpha\rho_v} \frac{n_0}{1 + n_0 \cdot 4\pi R^3/3} \frac{d}{dt} \left( \frac{4}{3} \pi R^3 \right) \end{aligned} \quad (9)$$

### 2.3. Turbulence modeling

As pointed out in our previous work [11], at present no appropriate turbulence models are available of addressing

TABLE I  
 Closure coefficients for turbulence modeling.

$\gamma$	$\beta_\omega$	$\beta_k$	$\sigma_\omega$	$\sigma_k$
0.52	0.072	0.09	0.5	0.5

the dispersed two-phase dynamics involved in this flow field. As a preliminary investigation, we apply the Wilcox  $k$ - $\omega$  model [6] of single phase flows to the simulation of cavitating flows:

- dynamic eddy viscosity  $\mu_t$ :

$$\mu_t = \frac{\rho k}{\omega} \quad (10)$$

- turbulence kinetic energy  $k$ :

$$\begin{aligned} \frac{\partial(\rho k)}{\partial t} + \frac{\partial(\rho k c_j)}{\partial x_j} &= \tau_{ij} \frac{\partial(\rho c_i)}{\partial x_j} - \rho \beta_k k \omega \\ &+ \frac{\partial}{\partial x_j} \left[ (\mu + \sigma_k \mu_t) \frac{\partial k}{\partial x_j} \right] \end{aligned} \quad (11)$$

- specific dissipation rate  $\omega$ :

$$\begin{aligned} \frac{\partial(\rho \omega)}{\partial t} + \frac{\partial(\rho \omega c_j)}{\partial x_j} &= \gamma \frac{\omega}{k} \tau_{ij} \frac{\partial(\rho c_i)}{\partial x_j} - \rho \beta_\omega \omega^2 \\ &+ \frac{\partial}{\partial x_j} \left[ (\mu + \sigma_\omega \mu_t) \frac{\partial \omega}{\partial x_j} \right] \end{aligned} \quad (12)$$

where the indices are  $i = 1, 2$  and  $j = 1, 2$  for 2D flow problems. The specific Reynolds stresses are given by

$$\tau_{ij} = -\frac{2}{3} \delta_{ij} \rho k + \mu_t \left( \frac{\partial \bar{c}_i}{\partial x_j} + \frac{\partial \bar{c}_j}{\partial x_i} \right) \quad (13)$$

where the Kronecker symbol  $\delta_{ij} = 1$  for  $i = j$ . The closure coefficients used in this study are listed in *table I*.

This  $k$ - $\omega$  model is applicable to both wall-bounded and free shear flows, see [6]. The later case will be simulated in the future. This model is able to obtain acceptable accurate results by integrating through the viscous sublayer [6]. However, at high Reynolds numbers, the viscous sublayer of a boundary layer is so thin that it is difficult to use enough grid points to resolve it. To reduce the computational time, we use wall functions. This procedure uses the law of the wall. In the law of the wall approach, the near wall tangential velocity is related to the wall shear stress by means of a logarithmic relation, which, in one standard form, can be written as follows:

$$u^+ = \frac{1}{\kappa} \ln(n^+) + C \quad (14)$$

 TABLE II  
 Empirical constants of the wall functions.

$\kappa$	$C$	$d_1$	$d_2$	$d_3$	$d_4$
0.41	5.2	$6.4262 \cdot 10^{-4}$	$-5.2113 \cdot 10^{-2}$	1.4729	-1.1422

where  $n^+$  is dimensionless distance from the wall surface which is defined as  $n^+ = nu_\tau/\nu$ ;  $u^+ = u_t/u_\tau$ ;  $u_\tau$  is the friction velocity constructed from the wall stress in the standard manner:  $u_\tau = \sqrt{\tau_{\text{wall}}/\rho}$ .  $u_t$  is the velocity component tangential to the wall and  $n$  the distance from the wall,  $\nu$  is the kinematic viscosity. In principle, the constant  $C$  varies for compressible flows, since it includes density and viscosity effects in the viscous wall region. However, correlation of measurements shows that  $\kappa$  and  $C$  are nearly the same as for incompressible boundary layers [12]. Therefore, the constants for incompressible flows are used here for cavitating flows.

The recommended practice is to locate near-wall nodes such that  $n^+$  is in the range of 30 to 500, for smooth walls. In general, some nodes might be located closer to the wall than a value of 30, where the logarithmic profile no longer holds. In this study, the near wall region is divided into three sections, and the associated relations are given below:

$$u^+ = \begin{cases} n^+ & \text{for } n^+ \leq 5 \\ d_1(n^+)^3 + d_2(n^+)^2 \\ \quad + d_3 n^+ + d_4 & \text{for } 5 < n^+ \leq 30 \\ \frac{1}{\kappa} \ln(n^+) + C & \text{for } n^+ > 30 \end{cases} \quad (15)$$

The relations are used to define the values of the energy production terms  $\tau_{ij} \partial(\rho c_i)/\partial x_j$  (see Eq. (11)) at the grid points closest to the wall surface, according to the distances  $n$  from the wall. Then the  $k$ -equation (Eq. (11)) is integrated up to the wall surface by setting  $k = 0$  at the wall and using the evaluated values of the energy production. As commonly, we also assume that the flow is in local equilibrium, meaning the dissipation and production are equal. The empirical constants of the wall functions used in [13, 14] are applied in this study and listed in *table II*. Unless stated otherwise, calculations are performed using the turbulence modeling.

## 2.4. Solution procedure and boundary conditions

The transport equation for the vapor fraction (Eq. (9)) is explicitly discretized. Its solution procedure is similar to the CICSAM (Compressive Interface Capturing

Scheme for Arbitrary Meshes) method [4]. However, because we treat the fluid as a homogeneous vapor–liquid mixture and do not capture sharp interfaces, the convective term of Eq. (9) is approximated with a hybrid method which combines central differencing and upwind differencing algorithms:

$$\alpha_{\text{cellface}} = \beta\alpha_{\text{upwind}} + (1 - \beta)\alpha_{\text{downwind}} \quad (16)$$

where the weighting factor  $\beta$  is set to be 0.75 in this study, instead of the CICSAM factor of [4]. The momentum equations are implicitly discretized, which are coupled with Eq. (8) via the SIMPLE algorithm similar to the solution procedure proposed in [15].

The formulation of the numerical solution procedure is based on a cell-centered Finite-Volume method for the variables, e.g.,  $u$ ,  $v$ ,  $p$ ,  $k$ ,  $\omega$ ,  $\alpha$ . The calculations are performed by first computing the vapor transportation (Eq. (9)) for the new time step, and then using the new vapor fraction, i.e., the new mixture density, to calculate the momentum equations of the flow via an iterative process.

The solution of the Navier–Stokes equations necessitates appropriate initial and boundary conditions to make the resulting system of algebraic equations solvable and the result unique. Since the effects of initial and boundary conditions may be remembered by the flow for a considerable time, they can have a significant influence on the results. Therefore, the initial and boundary conditions should be provided as realistic as possible. In this study a stationary single phase fluid is assumed as the initial condition. Both inflow and outflow boundaries are modeled as constant-pressure surfaces. At the inlet, the turbulence kinetic energy  $k$  is set to be equal to  $6 \cdot 10^{-4} u_{\text{in}}^2$ . The value of the specific dissipation rate  $\omega$  is selected using the length scale equation, see [14, 15]. On the wall, the boundary conditions are the impermeability and no-slip for the velocity, and the normal gradient of pressure is assumed to be zero. The wall functions are used as the wall boundary conditions for the turbulence modeling, see Section 2.3.

### 3. RESULTS

To validate our numerical scheme and study the physical effects concerning the cavitation in injector nozzles, 2D plane experimental test cases of Roosen et al. [16] are recalculated. The fluid used in the experiments was tap water. In this study calculations are carried out for water at room temperature (20 °C). The “bore hole” of

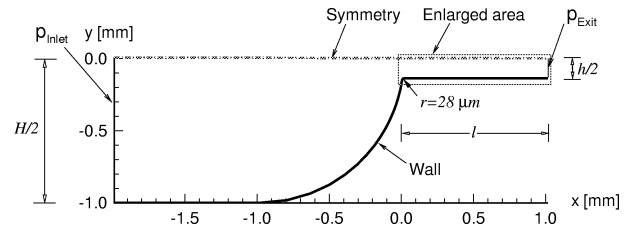
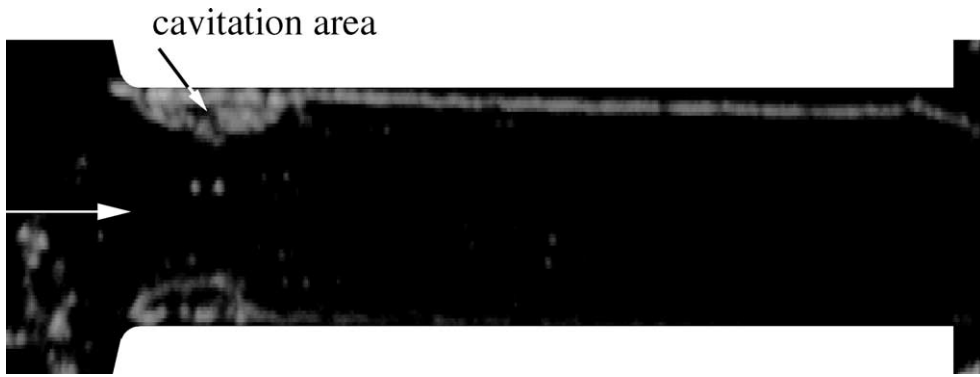


Figure 1. Lower half of the 2D plane injector nozzle.

the nozzle consists of a rectangular-shaped channel of  $0.2 \times 0.28 \times 1 \text{ mm}^3$  ( $w \times h \times l$ ). To reduce the computational time, we assume a 2D flow and symmetry with respect to the nozzle axis. Figure 1 shows the nozzle geometry and boundary conditions, corresponding to the experiments of Roosen et al. [16]. The radius of the nozzle lip was determined to be of the order of 25  $\mu\text{m}$  for the experiments [16]. Here, we assume a rounding of the lip with a radius of  $r = 0.1h = 28 \mu\text{m}$ . Unless stated otherwise, this radius is used for all simulations, except for the simulations of the effects of the lip rounding (Section 3.4). A computational mesh of  $95 \times 13$  nodes is used for the spatial discretization.

#### 3.1. Numerical estimation of an optimum nuclei concentration $n_0$

Euler solutions have shown that the nuclei concentration  $n_0$  must be at least of the order of  $10^{14} \text{ nuclei} \cdot \text{m}^{-3}_{\text{water}}$  to establish satisfying agreement with experiments, see [11]. In this study, we perform  $n_0$ -variation via turbulent Navier–Stokes simulations in order to match experimental observations for a given fluid (here water) at a given cavitation condition; then this value will be used to predict cavitation behavior at other conditions. The selected test case is that experimental case with  $p_{\text{Injection}} = 80 \text{ bar}$  and  $p_{\text{Exit}} = 21 \text{ bar}$  which is shown in figure 2. As in our previous work [11] for the laminar Navier–Stokes simulations, a nuclei radius  $R_0 = 0.3 \mu\text{m}$  is assumed in this study. In Section 3.2 it will be shown that this radius is in the insensitive range, meaning that the computed results are not depending on  $R_0$ . The calculations are performed with a time step  $\Delta t = 3 \cdot 10^{-8} \text{ s}$ , corresponding to a maximum CFL number of about 0.1–0.5. Figure 3 depicts the computed results for different nuclei concentrations. The computed result of the turbulent Navier–Stokes simulation using  $n_0 = 1.5 \cdot 10^{14} \text{ nuclei} \cdot \text{m}^{-3}_{\text{water}}$  yields a length of the cavitation region of about 200  $\mu\text{m}$ , which agrees well with the experimental observation of Roosen et al. [16]. For the remainder of this paper, the case with



**Figure 2.** Experimental density gradient distribution in the enlarged area of the nozzle for  $p_{\text{Injection}} = 80$  bar and  $p_{\text{Exit}} = 21$  bar, flow from left to right, from Roosen et al. [16].

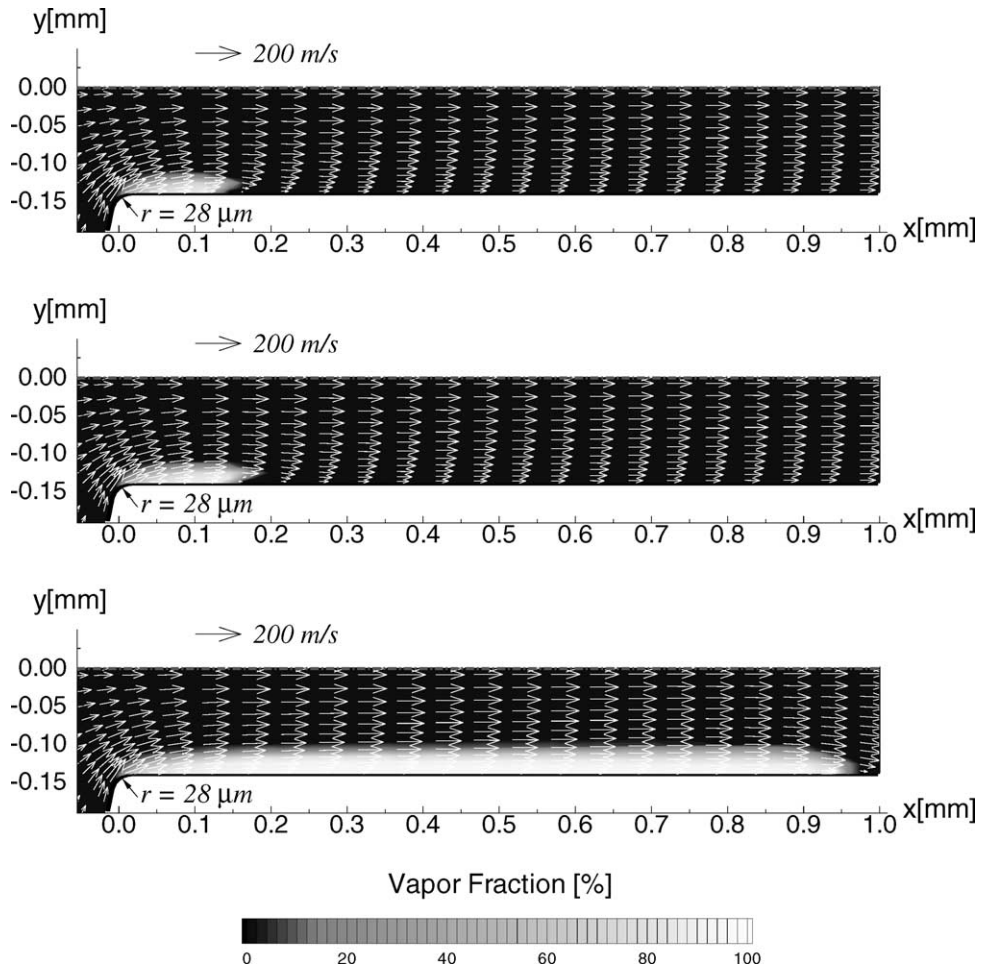


**Figure 3.** Computed steady vapor fraction distributions for different nuclei concentrations  $n_0$ . Turbulent Navier-Stokes solutions,  $p_{\text{Inlet}} = 80$  bar,  $p_{\text{Exit}} = 21$  bar,  $2.77 \cdot 10^4 \leq Re = \bar{u}_{\text{Inlet}} H / \nu \leq 2.80 \cdot 10^4$ ,  $R_0 = 0.3 \mu\text{m}$ . Top:  $n_0 = 1.0 \cdot 10^{14}$  nuclei  $\cdot \text{m}^{-3}_{\text{water}}$ ; middle:  $n_0 = 1.5 \cdot 10^{14}$  nuclei  $\cdot \text{m}^{-3}_{\text{water}}$ ; bottom:  $n_0 = 2.0 \cdot 10^{14}$  nuclei  $\cdot \text{m}^{-3}_{\text{water}}$ .

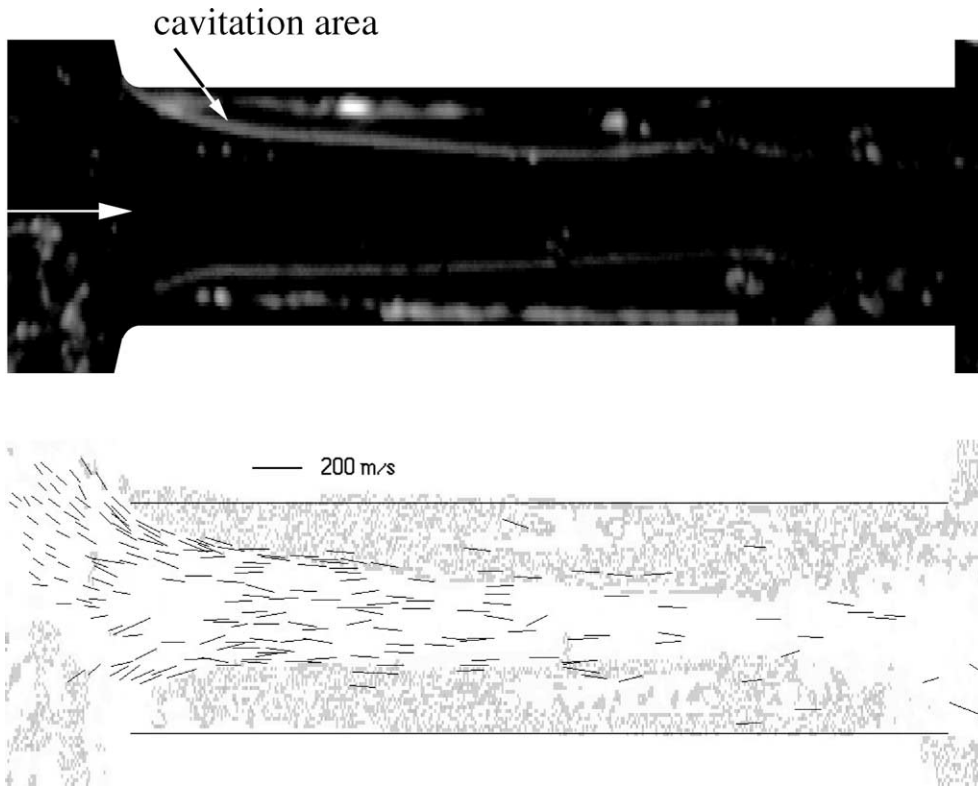


**Figure 4.** Experimental density gradient distribution (upper) and velocity distribution (lower) in the enlarged area of the nozzle for  $p_{\text{Injection}} = 80$  bar and  $p_{\text{Exit}} = 11$  bar, flow from left to right, from Roosen et al. [16].

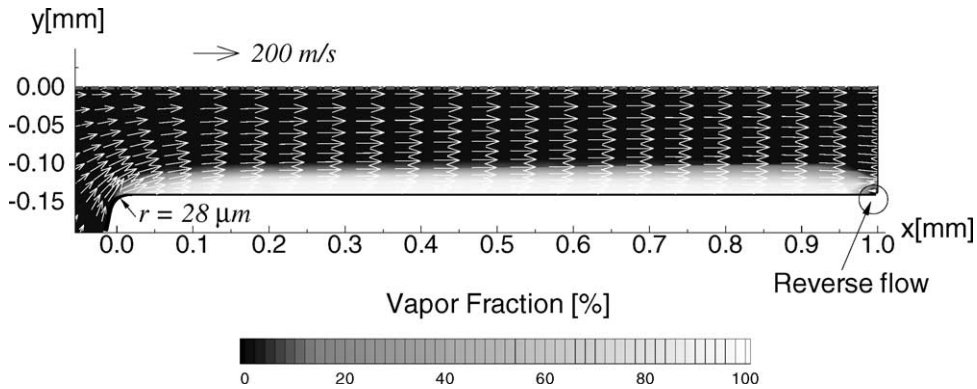


**Figure 5.** Plot of instantaneous unsteady vapor fraction distribution for  $p_{\text{Inlet}} = 80$  bar and  $p_{\text{Exit}} = 11$  bar. Turbulent Navier-Stokes solution,  $Re = \bar{u}_{\text{inlet}} H / \nu = 2.79 \cdot 10^4$ ,  $n_0 = 1.5 \cdot 10^{14}$  nuclei  $\cdot$  m $^{-3}_{\text{water}}$ ,  $R_0 = 0.3 \mu\text{m}$ ,  $r = 28 \mu\text{m}$ ,  $f = 127.2$  kHz.

$n_0 = 1.5 \cdot 10^{14}$  nuclei  $\cdot$  m $^{-3}_{\text{water}}$ ,  $R_0 = 0.3 \mu\text{m}$ ,  $r = 28 \mu\text{m}$ ,  $p_{\text{Inlet}} = 80$  bar,  $p_{\text{Exit}} = 21$  bar will be referred as the reference case.

To verify the reliability of the above numerically determined nuclei concentration, another test case of  $p_{\text{Injection}} = 80$  bar and  $p_{\text{Exit}} = 11$  bar is recalculated. *Figure 4* shows the experimental density gradient and the

velocity distribution in the nozzle measured by Roosen et al. [16]. *Figure 5* indicates that the computed result using  $n_0 = 1.5 \cdot 10^{14}$  nuclei  $\cdot$  m $^{-3}_{\text{water}}$  gives a good agreement with the experiment.

As shown in *figure 5* a reverse flow may occur at the nozzle exit in the simulations, indicating a hydraulic flip

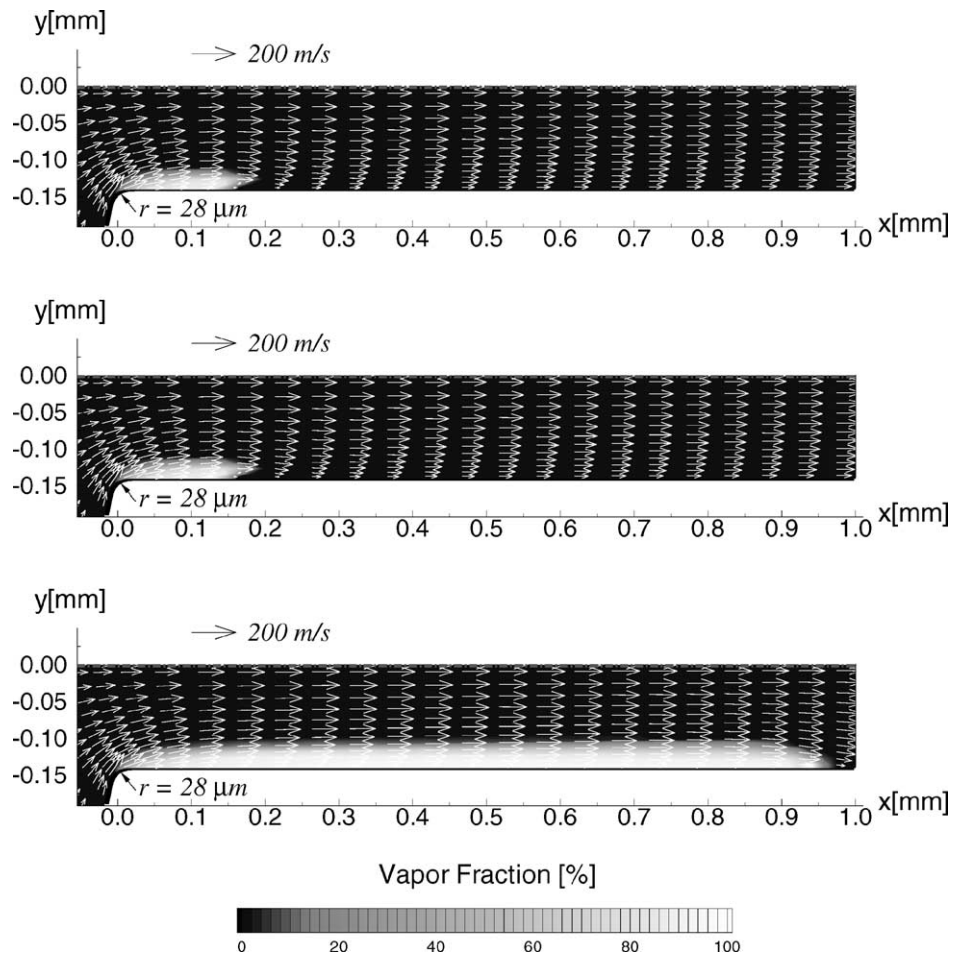


**Figure 6.** Computed steady vapor fraction distributions for different nuclei radii  $R_0$ . Turbulent Navier–Stokes solutions,  $p_{\text{inlet}} = 80$  bar,  $p_{\text{Exit}} = 21$  bar,  $2.78 \cdot 10^4 \leq Re = \bar{u}_{\text{inlet}} H / \nu \leq 2.79 \cdot 10^4$ ,  $n_0 = 1.5 \cdot 10^{14}$  nuclei·m $^{-3}$ <sub>water</sub>. Top:  $R_0 = 0.3$   $\mu\text{m}$ ; middle:  $R_0 = 1.2$   $\mu\text{m}$ ; bottom:  $R_0 = 1.5$   $\mu\text{m}$ .

situation which was first introduced in [2]. In this situation, one needs to specify the vapor fraction at the boundary points where the reverse flows occur, to continue the calculation. In the work [17] it was presumed that the higher-pressure gases could come into the low-pressure region. In another work [18] the calculation proceeded as if the nozzle were submerged in fuel, rather than injecting into a gaseous atmosphere. In this study, pure liquid ( $\alpha = 0$ ) is assumed for the reverse flow. A periodic unsteady behavior of the flow field is obtained. *Figure 5* shows a plot of the vapor fraction distribution of this unsteady flow. In this unsteady situation the location of the cavitation “wake” oscillates slightly and the total vapor fraction in the nozzle changes with a frequency of  $f = 127.2$  kHz. This cavitating flow with a reverse flow

at the nozzle exit will be further investigated by coupling the calculation of the external flow in the future.

### 3.2. Effect of liquid quality

The liquid quality may be described by the nuclei concentration and the nuclei radii. The effect of the nuclei concentration has been shown in *figure 3*. Theoretically, the nuclei radius  $R_0$  may play an important role too, because the nuclei radius  $R_0$  influences the vapor production where the static pressure first drops under the equilibrium vapor pressure. To identify the effect of the nuclei radius  $R_0$ , four simulations for different nuclei radii  $R_0 = 0.03, 0.3, 1.2$  and  $1.5$   $\mu\text{m}$  are performed. The computed vapor fraction distributions are shown in *figure 6*.

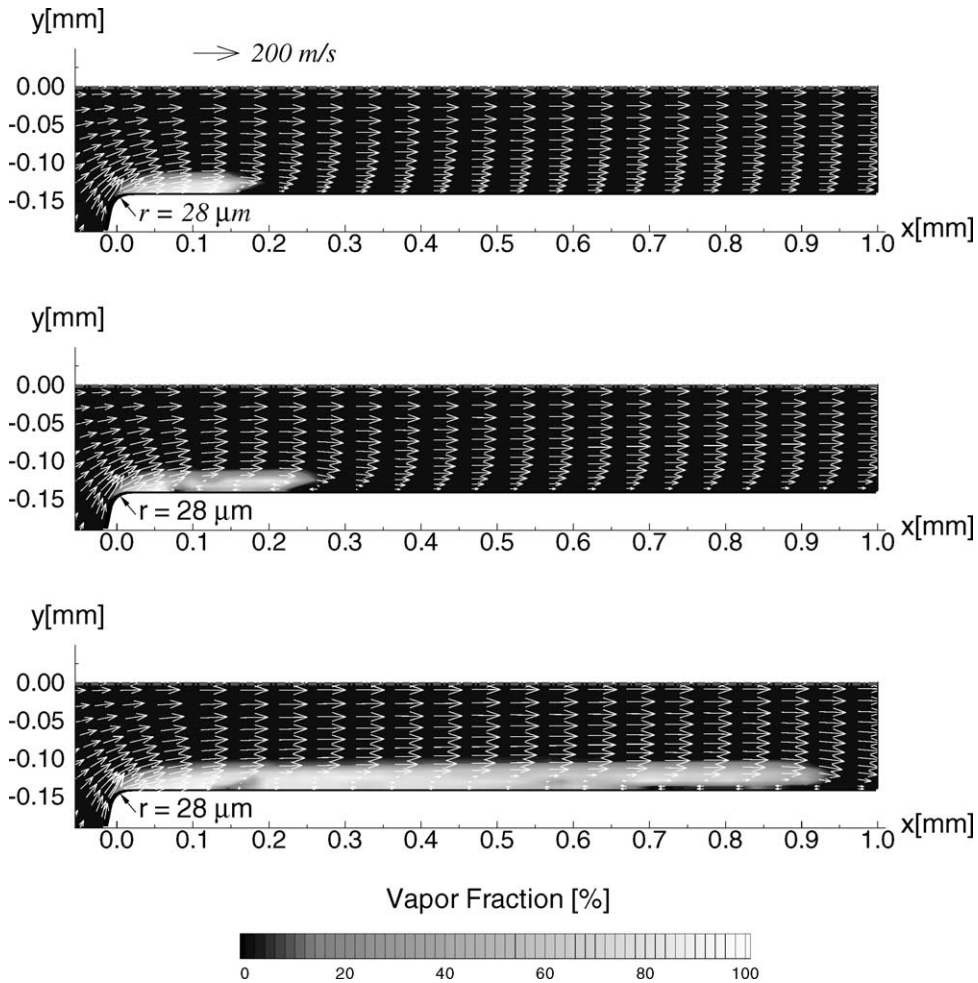


**Figure 7.** Computed steady vapor fraction of viscous and inviscid solutions.  $p_{\text{Inlet}} = 80$  bar and  $p_{\text{Exit}} = 21$  bar,  $n_0 = 1.5 \cdot 10^{14}$  nuclei  $\cdot \text{m}^{-3}$ ,  $R_0 = 0.3 \mu\text{m}$ . Top: turbulent Navier–Stokes solution,  $Re = \bar{u}_{\text{Inlet}} H / \nu = 2.78 \cdot 10^4$ ; middle: laminar Navier–Stokes solution,  $Re = \bar{u}_{\text{Inlet}} H / \nu = 2.74 \cdot 10^4$ ; bottom: Euler solution,  $Re = \bar{u}_{\text{Inlet}} H / \nu = 2.76 \cdot 10^4$ .

There are slight differences of the vapor fraction distributions among the cases  $R_0 = 0.03, 0.3$  and  $1.2 \mu\text{m}$ , which indicates that the computed results are not sensitive to radius variation between  $0.03$  and  $1.2 \mu\text{m}$ . However, the two-phase region in the case  $R_0 = 1.5 \mu\text{m}$  is much larger. This can be interpreted by analyzing the vapor transport equation (Eq. (9)). In the case  $R_0 \leq 1.2 \mu\text{m}$ , the vapor productions in cells where the static pressure first drops under the equilibrium vapor pressure are not large enough to balance the convective effect. Thus, the vapor fractions as well as the “bubble” radii do not grow in these cells. In contrast to the cases  $R_0 \leq 1.2 \mu\text{m}$ , in the case  $R_0 = 1.5 \mu\text{m}$  the source term becomes much larger, such that it plays a more important role than the convective term. This yields quantitatively positive effects on the va-

por convective transport and growth in the downstream region. An optimum combination of  $n_0$  and  $R_0$  will be further investigated.

### 3.3. Effect of viscosity and turbulence

To demonstrate the effects of the viscosity and the turbulence, a Euler solution as well as a laminar solution are performed for the reference geometry. *Figure 7* shows that the cavitation region of the Euler solution is much larger than those of Navier–Stokes solutions. This is because the primary role of viscosity in this flow is to increase dissipation and flow losses downstream of the contraction at the nozzle throat. Due to the

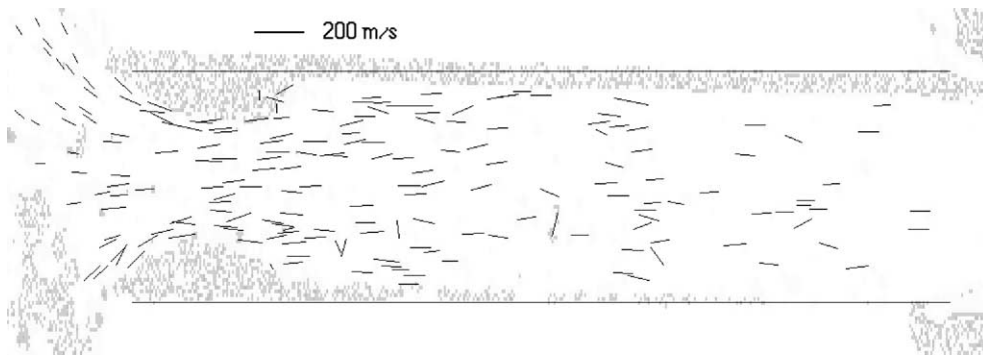


**Figure 8.** Experimental velocity distribution in the enlarged area of the nozzle for  $p_{\text{Injection}} = 80$  bar and  $p_{\text{Exit}} = 21$  bar, flow from left to right, from Roosen et al. [16].

viscous dissipation the vapor fraction is transported more slowly, therefore the two-phase regions of the Navier–Stokes simulations are smaller. The comparison with the experimental velocity distribution (*figure 8*) indicates that the turbulent Navier–Stokes simulation yields the best agreement with the experiment.

### 3.4. Influence of the lip rounding

Calculations are performed for different radii at the nozzle throat. *Figure 9* shows the effects of the nozzle lip rounding on the cavitation behavior. As expected, the cavitation regions in the cases with bigger radii  $r$  of the rounding are smaller. In addition, the simulation in the sharp-edged case ( $r = 0 \mu\text{m}$ ) gives the largest total vapor fraction which is about 20% larger than that in the case of  $r = 14 \mu\text{m}$ . This means that the rounding of the nozzle lip serves to inhibit cavitation.

### 3.5. Interaction between flow separation and cavitation

As shown in *figure 9*, the length of the two-phase flow region in the case of  $r = 0 \mu\text{m}$  is shorter than that in the case of  $r = 14 \mu\text{m}$ . This interesting phenomenon is most probably a result of the effect of the separation of the primary fluid on the cavitation. To clarify this effect, the stream lines of the simulations for single phase flows are shown in *figure 10*. In the case of  $r = 0 \mu\text{m}$ , the single phase flow does separate. In the cavitation situation, the reverse flow originally formed by the separation of the primary flow due to the nozzle lip sharpness brings the liquid towards the two-phase region, which affects the

vapor convective transport and forces the two-phase flow region to become shorter.

This effect of the separation on the cavitation can also be verified by a comparison of the turbulent simulation and the laminar simulation for the sharp-edged case. The separation region of the laminar simulation for the single phase flow is larger than that of the turbulent simulation, but the calculated cavitation regions are exactly the opposite. The vapor fraction distribution of the laminar solution using  $n_0 = 1.5 \cdot 10^{14} \text{ nuclei} \cdot \text{m}^{-3}_{\text{water}}$  is similar to that using  $n_0 = 1 \cdot 10^{17} \text{ nuclei} \cdot \text{m}^{-3}_{\text{water}}$  with a few differences. The latter can be found in [11]. Note that, the laminar solutions for the sharp-edged case are unsteady. In contrast, the total vapor content in the nozzle of the turbulent solution is in a steady state. This difference is generated due to the effect of the eddy viscosity introduced in the turbulence modeling. The eddy viscosity is very large compared to the molecular viscosity, which damps the unsteadiness occurred in the laminar simulations.

On the other hand, the cavitation process may result in flow separation. *Figure 10* shows that no separation occurs in the single phase flow simulations in the case with the reference geometry ( $r = 28 \mu\text{m}$ ). However, *figure 7* indicates that the cavitating flows do separate. This implies that the separation of the cavitating flow is not necessarily formed by the primary single phase flow, but by the cavitation process. A reverse flow in the cavitation region may occur due to the lower pressure in the cavitation region which leads to a positive pressure gradient in the wake region of the cavitation. Furthermore, the separation region of this cavitating flow is slightly larger than the two-phase flow region. Because the cavitating flow may separate, therefore, Euler solutions and laminar solutions are no longer appropriate to the simulation of cavitating flows.

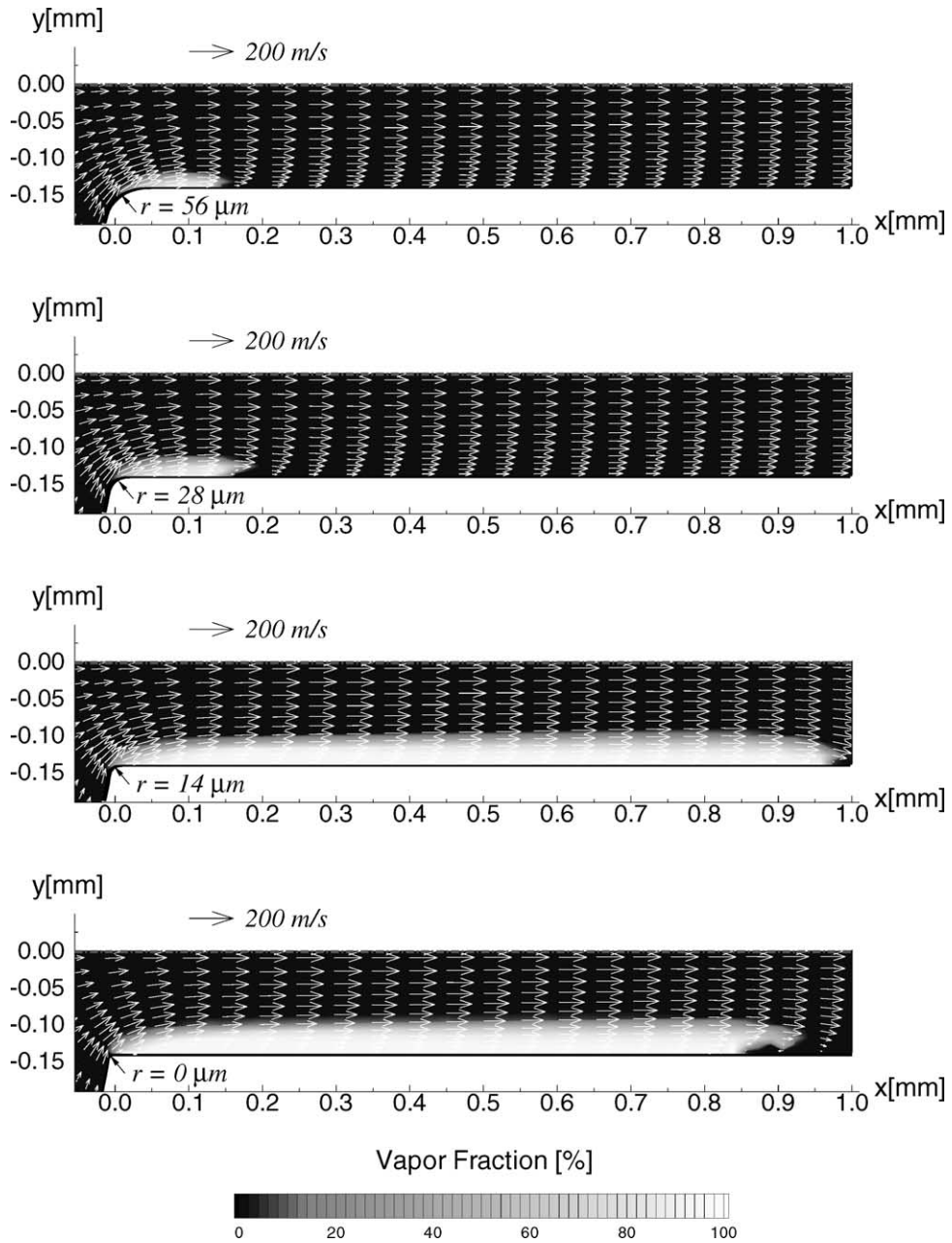


**Figure 9.** Computed steady vapor fraction distributions for different lip roundings  $r$ . Turbulent Navier–Stokes solutions,  $p_{\text{inlet}} = 80$  bar,  $p_{\text{Exit}} = 21$  bar,  $n_0 = 1.5 \cdot 10^{14}$  nuclei  $\cdot \text{m}^{-3}$ ,  $R_0 = 0.3 \mu\text{m}$ . Top:  $r = 0.2h = 56 \mu\text{m}$ ,  $Re = \bar{u}_{\text{inlet}} H / \nu = 2.84 \cdot 10^4$ ; next to top:  $r = 0.1h = 28 \mu\text{m}$ ,  $Re = \bar{u}_{\text{inlet}} H / \nu = 2.78 \cdot 10^4$ ; next to bottom:  $r = 0.05h = 14 \mu\text{m}$ ,  $Re = \bar{u}_{\text{inlet}} H / \nu = 2.67 \cdot 10^4$ ; bottom:  $r = 0 \mu\text{m}$ ,  $Re = \bar{u}_{\text{inlet}} H / \nu = 2.50 \cdot 10^4$ .

#### 4. CONCLUSIONS

A numerical model has been developed to investigate steady or unsteady cavitation processes in injector nozzles in a time accurate manner. The model includes vis-

cous and turbulent effects, as well as a new constitutive relation required for the mixture density which is a part of the two-phase formulation.

The numerical study of a symmetric injection nozzle has identified several complex phenomena which cer-

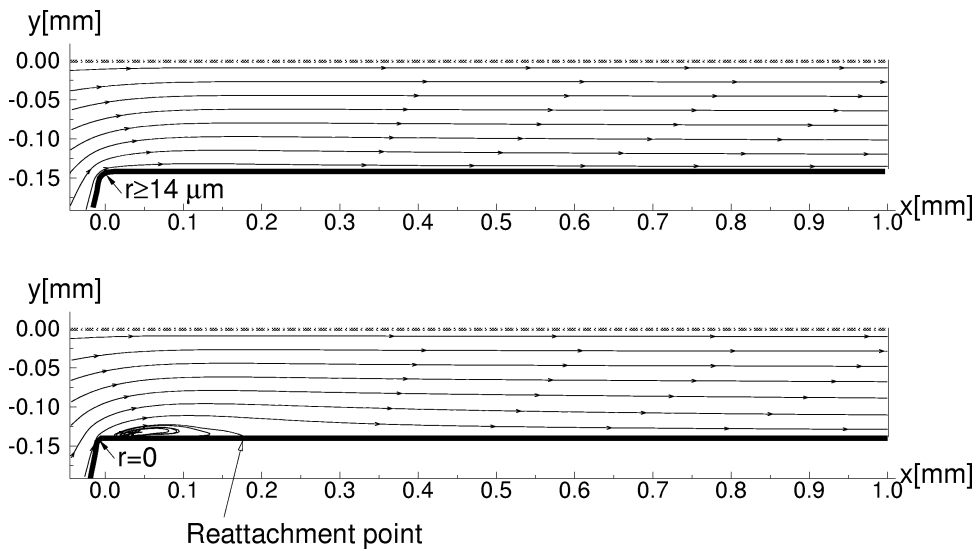


**Figure 10.** Stream lines of single phase flows for  $p_{\text{Inlet}} = 80$  bar and  $p_{\text{Exit}} = 21$  bar. Turbulent Navier-Stokes solutions. Upper:  $r = 14 \mu\text{m}$ ,  $Re = \bar{u}_{\text{Inlet}} H / \nu = 2.79 \cdot 10^4$ ; lower:  $r = 0 \mu\text{m}$ ,  $Re = \bar{u}_{\text{Inlet}} H / \nu = 2.52 \cdot 10^4$ .

tainly occur inside fuel injector nozzles. Numerical results indicate that the overall extension of the cavitation region depends on the liquid quality and the nozzle pressure difference, i.e. the higher nuclei concentration and the bigger nuclei radii as well as the lower pressure at the nozzle exit cause larger overall extension of the cavitation. The numerical study also demonstrates that the rounding of the nozzle inlet lip tends to inhibit the overall extension of the cavitated region. At the same time, the numerical simulations point out that the flow separation in injector nozzles may be caused due to the sharpness of the nozzle inlet lip as well as by the cavitation process. The separation formed by the primary single flow influences the extension of the two-phase region. To simulate the interaction between the flow separation and the flow cavitation more accurately, the turbulence model will be improved.

### Acknowledgements

The authors gratefully acknowledge the support from the Deutsche Forschungsgemeinschaft under Grant Schn-352/16-1 during performing this work. Sincere thanks are given to Dr.-Ing. P. Roosen and Dipl.-Ing. O. Genge of the Institute for Technical Thermodynamics of the RWTH Aachen (Germany) for providing the experimental data.

### REFERENCES

- [1] Kluitmann S., Roosen P., Knoche K.F., Untersuchung und Modellierung des transienten Verhaltens von Kavitationserscheinungen bei ein- und mehrkomponentigen Kraftstoffen in schnell durchströmten Düsen, Report of the Institute for Technical Thermodynamics, RWTH Aachen (Univ. of Tech.), Germany, April 1994.
- [2] Bergwerk W., Flow pattern in diesel nozzle spray holes, Proceedings of the Institute on Mechanical Engineers 173 (25) (1959) 655–660.
- [3] Hirt C.W., Nichols B.D., Volume of fluid (VOF) method for the dynamics of free boundaries, Journal of Computational Physics 39 (1981) 201–225.
- [4] Ubbink O., Numerical prediction of two fluid systems with sharp interfaces, Ph.D. thesis, University of London, 1997.
- [5] Rayleigh L., On the pressure developed during the collapse of a spherical cavity, Phil. Mag. S. 6 34 (200) (1917) 94–98.
- [6] Wilcox D.C., Turbulence Modeling for CFD, DCW Industries, Inc., La Canãda, CA, 1998.
- [7] Sauer J., Schnerr G.H., Unsteady cavitating flow — A new cavitation model based on a modified front capturing method and bubble dynamics, in: Proceedings of 2000 ASME Fluid Engineering Summer Conference, Boston, MA, June 11–15, 2000.
- [8] Plesset M.S., Cavitating flows, Report No. 85-46, Division of Engineering and Applied Science, California Institute of Technology, Pasadena, CA, April 1969.
- [9] FLUENT 5: User's Guide Volume 3 — Draft, April 12, 1999.
- [10] Spalding D.B., A method for computing steady and unsteady flows possessing discontinuities of density, CHAM report 910/2, 1974.
- [11] Yuan W., Sauer J., Schnerr G.H., Modeling of unsteady cavitating flows in fuel injection nozzles, in: ILASS-Europe 2000, Darmstadt, 11–13 September 2000.

- [12] Bradshaw P., Huang G.P., The law of the wall in turbulent flow, *P. Roy. Soc. Lond. A* 451 (1995) 165–188.
- [13] TASCflow (ASC), Theory Documentation, Version 2.4, Waterloo, ON, Canada, 1995.
- [14] Yuan W., Schilling R., Numerical simulation of the draft tube and tailwater flow interaction, *Journal of Hydraulic Research* (accepted for publication).
- [15] Ferziger J.H., Perić M., *Computational Methods for Fluid Dynamics*, Springer-Verlag, Berlin/Heidelberg, 1996.
- [16] Roosen P., Unruh O., Behmann M., Untersuchung und Modellierung des transienten Verhaltens von Kavitationserscheinungen bei ein- und mehrkomponentigen Kraftstoffen in schnell durchströmten Düsen, Report of the Institute for Technical Thermodynamics, RWTH Aachen (Univ. of Tech.), Germany, March 1996.
- [17] Chen Y., Heister S.D., Modeling cavitating flows in diesel injectors, *Atomization and Sprays* 6 (1996) 709–726.
- [18] Schmidt D.P., Rutland C.J., Corradini M.L., Roosen P., Genge O., Cavitation in two-dimensional asymmetric nozzles, in: *International Congress and Exposition*, Detroit, MI, March 1–4, 1999, SAE technical paper 1999-01-0518.
- [19] Schnerr G.H., Vortmann C., Sauer J., Numerical studies of flow in fuel injector nozzles—Interaction of separation and cavitation, in: *Mayinger F., Giernoth B. (Eds.), DFG-Schwerpunktprogramm “Transient Phenomena in Multiphase and Multicomponent Systems”*, Wiley-VCH, Weinheim, 1999, pp. 335–350.